Neuromorphic Visual Artificial Synapse In-memory Computing Systems based on GeO_x-coated MXene Nanosheets

Yixin Cao[1,2,‡], Tianshi Zhao[1,2,‡], Chenguang Liu[1,‡], Chun Zhao[1,2,], Hao Gao[3], Shichen Huang[1], Xianyao Li[1], Chengbo Wang[1], Yina Liu[4], Eng Gee Lim[1,*] and Zhen Wen[5,*]*

[1] School of Advanced Technology, School of Science, School of Robotics, Xi'an Jiaotong-Liverpool University, Suzhou 215123, China

[2] Department of Electrical Engineering and Electronics, University of Liverpool, Liverpool L69 3GJ, UK

[3] Department of Electrical Engineering, Eindhoven University of Technology, Eindhoven, Netherlands

[4] Department of Applied Mathematics, School of Mathematics and Physics, Xi'an Jiaotong-Liverpool University, Suzhou 215123, China.

[5] Institute of Functional Nano and Soft Materials (FUNSOM), Jiangsu Key Laboratory for Carbon-Based Functional Materials and Devices, Soochow University, Suzhou 215123, China.

Corresponding Authors: chun.zhao@xjtlu.edu.cn (C. Zhao), enggee.lim@xjtlu.edu.cn (E. G. Lim), wenzhen2011@suda.edu.cn (Z. Wen)

[‡] These authors contributed equally to this work.

Abstract

Artificial synapses with light signal perception capability offer the ability to neuromorphic visual signal processing system on demand. In light of the excellent optical and electrical characteristics, the low-dimensional materials have become one of the most favorable candidates of the key component for optoelectronic artificial synapses. Previously, our group originally proposed the synthesis of germanium oxide-coated MXene nanosheets. In this work, we further applied this technology into the optoelectronic synaptic thin-film transistors for the first time. The devices exhibited the adjustable postsynaptic current behaviors under the visible light inputs. Moreover, the potentiation and depression operation modes of the devices further improved the application potential of the devices in mimicking biological synapses. Regulated by the wavelength of incident lights, the proposed artificial synapse could effectively help detect the target area of the image. Eventually, we further showed the results of the devices in the projects of neural network computing task. The long-term potentiation/depression characteristics of the conductance were applied to the synaptic weight matrix for image identification and path recognition tasks. By adding knowledge transfer in the process of recognition, the epoch required for convergence has been greatly reduced. The result of high noise tolerance revealed the great potential of the proposed transistors in establishing high-efficiency and robustness hardware neuromorphic systems for in-memory computing.

Keywords: artificial synapse, MXene, visible light detection, in-memory computing, neural circuit policies

1. Introduction

The in-memory neuromorphic devices have shown great potential in the field of high-parallel big data computing applications based on neural network system[1-8]. Since 1948, the artificial synapses with biological synaptic behaviors have been proved to be one of the leading directions in the research of neuromorphic devices[9-13]. Typically, the unit synaptic device could transfer the signals between pre- and postsynaptic terminals, as the neurons in a biological nervous system, during which the input stimuli could be processed into the output response with neuronal plasticity[4, 6, 14-16]. One neuromorphic computing array could contain plenty of artificial synapses with highly parallel non-von Neumann architecture[5, 6, 9, 17]. Further, the energy consumption of one artificial device has been reported to be very low, approaching or even below the biological synapse (~10 fJ for one synaptic affair) [6, 14, 18, 19]. All these advantages indicate that the artificial synapses are suitable for human-like sensory information processing or other applications based on complex neuromorphic network structure[5, 17]. Especially for the three-terminal transistor-like synaptic devices, the voltage applied on the gate electrode (V_{GS}) is regarded as the presynaptic voltage (V_{pre}) and the drain current (I_{DS}) as the output, also named postsynaptic current (PSC)[20, 21]. Since the output response could be monitored as the input signal is applied, the synaptic transistors are considered to have excellent applicability for mimicking neural behaviors[20, 22, 23].

Among a number of artificial synaptic devices, photoelectric synaptic devices stand out due to their low power consumption, small mutual interference of optical input signals, and more conducive to high-speed and high-density processing of large amounts of information[24, 25]. In addition, optoelectronic synaptic transistors are also of great significance for visual perception simulation and computer vision tasks[5, 26].

Recently, two-dimensional (2D) materials have been widely studied for optoelectronic applications due to their extraordinary physicochemical advantages such as thickness-dependent bandgap, high carrier mobility, and the wide optical absorption range covered from ultraviolet (UV) to terahertz[2, 27-33]. As an innovative 2D material, the MXene has been demonstrated to have its attractive behaviors like metallic conductivity, excellent hydrophilicity, and high optical transparency (>97% per nm), etc[34-36]. In particular, unlike the classical chemical vapor deposition (CVD)-processed 2D materials such graphene, MoS_2, and hBN, etc., MXene has distinguished compatibility with low or room temperature solution fabrication process, indicating a great application potential in the large-scale fabrication and flexible circuit production[36-39]. Moreover, previous studies have reported the good characteristics of MXene as a floating gate in the synaptic transistors and the optoelectric applications under UV light irradiation[34, 40, 41]. However, the application of MXene in the field of optoelectric synaptic transistors is still facing a bottleneck of working under the incident visible light (wavelength from 780 nm to 400 nm), which limits the further application in the field of visual perception[42]. Therefore, a feasible solution to overcome this is worth researching. Previously, our group initially reported a 2D nanosheet fabricated by a facile route of coating the MXene nanosheet with an ultra-thin layer of germanium oxide (GeO_x)[43]. Such nanosheets contain a large number of oxygen vacancies (V_o), and a heterostructure could be formed at the interface between them and other metal oxides, which all contribute to the current response under visible light incidence [43-45]. This provides a feasible solution for improving visible light response of synaptic devices based on 2D materials.

In this study, we present a kind of photonic synaptic thin-film transistors (TFTs) compatible with visible light stimuli. For the first time, the GeO_x-coated $Ti_3C_2T_x$

MXene (GMX) nanosheet was applied to the fabrication of GMX-based synaptic TFTs (GMXSTs). Combining the GMX with the n-type solution-processed zinc tin oxide (ZTO) together, a heterostructure was formed and provided the foundation of photoelectric response. The MXene also played an important role in optimizing the electron storage performance and enlarging the light-receiving area. The devices exhibited typical synaptic plasticity under both the V_{GS} pulses and the visible light stimuli. Then, we applied the various responses of the devices under the different input lights into image target area detecting simulations, indicating the visual perception mimicking capability. With the help of the detecting pre-process, the task of counting the fluorescent cells stained by 2-(4-Amidinophenyl)-6-indolecarbamidine dihydrochloride (DAPI) was correctly performed. Furthermore, based on the mixed light-voltage stimulated long-term potentiation/depression (LTP/D), the artificial neural network (ANN)-based classifier for digital images based on the Modified National Institute of Standards and Technology (MNIST) database was successfully established with noise tolerance close to the human eye. In addition, due to the addition of a knowledge transfer step in the process of recognition to use the pre-trained high-performance teacher network to guide the low-accuracy student network, the epoch required for convergence has been significantly reduced. Finally, for a more advanced path recognition task related to the automatic driving, the performance of GMXSTs was applied to a neural circuit policies (NCP) network. The successful obstacle-detecting result under Gaussian noise demonstrated the robustness of the NLP-based neural network system, indicating a bright future in the field of in-memory computing.

2. Results and Discussion

In human brain, there are billions of neurons with specific functions to sustain our body's activities, as depicted in **Figure 1**(a). Through the processes of receiving the

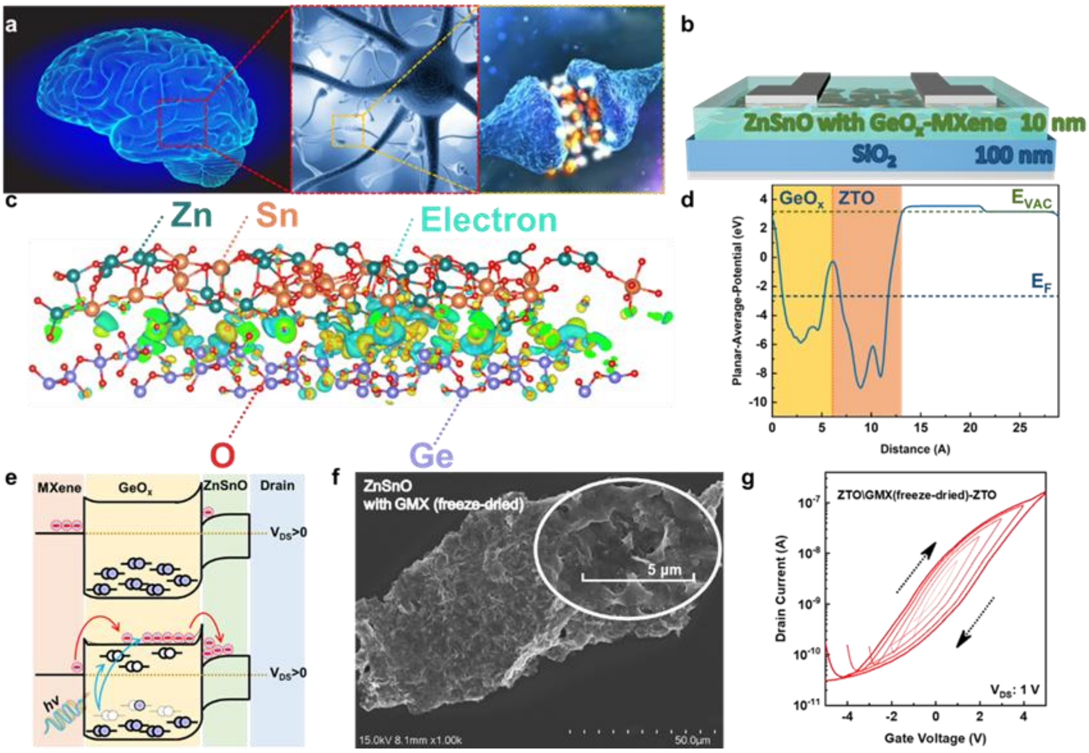

Figure 1. TFT design and material characterization. (a) Schematic diagram of biological visual perception nerve cells. (b) Conceptual diagram of simulating human visual perception through GMXSTs. (c) DFT calculation model diagram of GeO_x/ZTO heterostructure, revealing the first-principles optimized structure and electron density. (d) Charge density difference result of GeO_x/ZTO heterostructure in DFT calculation. (e) Energy band diagram of the photocurrent generated within the GMX/ZTO heterostructure. (f) Morphology of GMX prepared by freeze-drying in ZTO film, characterized by SEM. (g) GMXSTs transfer characteristic curve of the optimized channel structure.

signals, converting them into electrical signals, and delivering the signals to the brain through the synapses between the neurons, one can effectively capture the information and respond accordingly. Here, as shown in **Figure 1**(b), the TFTs with solution-processed GMX incorporated ZTO were fabricated to mimic the visual perception activity. The devices include a bottom gate of n^{++} heavily doped silicon (Si), a dielectric of silicon dioxide (SiO_2), an n-type channel layer of GMX doped ZTO, and the source (S)/drain (D) electrodes of aluminum (Al), which are described detailly in the 'Experimental' section. When an incident optical signal was applied to the device, the positive photocurrents, also regarded as the excitatory postsynaptic current excitatory postsynaptic current (EPSC), were generated in the channel, which is similar to the electrical signal conversion process in the visual system. Moreover, the photocurrent exhibited non-volatile behavior, which could mimic the memory property of the biological neurons.

Figure S1 introduces the synthesis process from MXene to GMX, where the coated polyvinyl pyrrolidone (PVP) interconnected with the MXene's surface providing a template for the growth of GeO_x [43]. The in-situ reduction caused by sodium borohydride ($NaBH_4$) led to a decrease in the valence state of Ge^{4+} and a formation of V_o [43]. The chemical bonds information measured by X-ray photoelectron spectroscopy (XPS) are displayed in Figure S2 and Figure S3, revealing the existence of MXene core (Ti 2*p* spectra) and the reduction of Ge^{4+} (Ge 3*d* spectra) [43]. Especially for the O 1*s* test results for the comparison between GeO_x and ZTO samples, a much higher content of V_o could be observed in GeO_x. According to the previous studies, the difference in V_o content in GeO_x and ZTO layers and the heterostructure formed between them are beneficial to the generation of photocurrent [46]. In order to further understand the microscopic properties and band structure of GeO_x/ZTO, we performed density functional theory (DFT) simulation, as the schematic diagram of structure and energy band distribution diagram displayed in **Figure 1**(c) and (d), respectively. In the DFT calculation, the layers of GeO_x and ZTO were assumed to be amorphous according to our previous researches [43, 47]. The high density of electron at the interface resulted from the barriers between the two materials, while the dense defect levels plotted in Figure S4 were majorly formed by the high concentration of V_o in the GeO_x.

Therefore, the generation of persistent photoconductivity (PPC) could be proposed and attributed to two core factors: (i) the existence of a large amount of V_o in GeO_x and

(ii) the trapping effect of GMX/ZTO heterostructures on carriers. As illustrated in the energy band diagram in **Figure 1**(e), the incident light excites the intrinsic V_o in GeO_x into V_o^{2+} and electrons narrow down the barriers between MXene/GeO_x and GeO_x/ZTO, so that more electrons are driven by the positive drain voltage (V_{DS}) to enter the ZTO channel and cause current increase [44, 45]. The potential well between the GeO_x and ZTO layers would subsequently trap the electrons and lead to the maintenance of carrier concentration rise after the disappearance of the light input [44, 45]. In addition to providing more electrons, the MXene core can also increase the surface area of GMX that receives light, which could further be improved through a freeze-dried process as shown in **Figure 1**(f) and Figure S5. We compared scanning electron microscope (SEM) results of the pure ZTO film and the ZTO films with GeO_x, thermal dried GMX, and freeze-dried GMX incorporation. It could be obviously observed that the freeze-dried GMX nanosheet exhibited the best malleability, which benefits the photon reception-response process. The high-resolution transmission electron microscopy (HR-TEM) in Figure S6 further confirmed the alternative composite structure. Figure S6a shows the GMX nanosheets are slightly stacked and uniformly distributed in the field of view. The TEM image of GMX (Figure S6b) further illustrates the successful integration, in which amorphous GeO_x is tightly coated on the MXene film with the unique layered structure of MXene sheets. The energy-dispersive X-ray spectroscopy (EDS) spectrum of the obtained GMX nanosheets (Figure S6c) also shows the uniform distribution of Ti, C, Ge, and O on the composite, indicating that GeO_x grows uniformly on the MXene sheets through the self-assembly process and in-situ reduction.

Figure 1(g) and Figure S7 summarize the transfer behaviors of the optimal device (double layered channel of ZTO\freeze-dried GMX doped ZTO, ZTO\GMX(freeze-dried)-ZTO) and the other control groups. It could be observed that the TFTs with single-layered pure ZTO channels have negligible hysteresis, indicating a high-quality film but not suitable for synaptic transistors. Typically, the hysteresis serves as the memory window of the synaptic transistors and leads to the non-volatile EPSC behavior [34]. For the GeO_x-ZTO devices, the large clusters of GeO_x formed in the film (Figure S5(b)) lead to a loose and porous structure, which is not conducive to electron conduction and lower down the current. Therefore, we choose the ZTO\GMX(freeze-dried)-ZTO channel-based TFTs as the optimal device and represent the GMXSTs. Figure S8 shows the transfer curve's variation of the GMXSTs under light conditions. Under the irradiation of red (660 nm, 23 mW/cm^2), green (520 nm, 22 mW/cm^2), and blue (450 nm, 15 mW/cm^2) (RGB) visible light, the I_{DS} of the devices showed a significant increase, which laid the foundation for subsequent research on visible light artificial synapses.

Based on the phenomenon of rising drain current caused by RGB light, we further test the photo-induced synaptic behaviors of the GMXSTs. Figure S9 shows the EPSC of the devices under one RGB light pulse. Since the photon energy of the three incident lights was different, blue light led to the largest output current, followed by green light, and red light caused the smallest current. EPSC did not disappear with the disappearance of light input, indicating that the current gain generated by light is non-volatile. **Figure 2**(a) depicts the paired-pulse facilitation (PPF) of the GMXSTs, which was tested under dual RGB light spikes with different time intervals (Δt) and utilized to reveal the device's basic synaptic behavior. Since it takes time for the recovery of the increased EPSC, the amplitude of the second EPSC peaks (A2) induced by the light spike were larger than the first ones (A1) at a small enough Δt value for all of the RGB incident lights. As shown in PPF index curve, the index can be fitted using function:

$$PPF\ index = A_2/A_1 = 1 + C_1 \exp(-\Delta t/\tau_1) + C_2 \exp(-\Delta t/\tau_2)$$

Where A_1 and A_2 are the first and second EPSC peaks, C_1 and C_2 are the initial

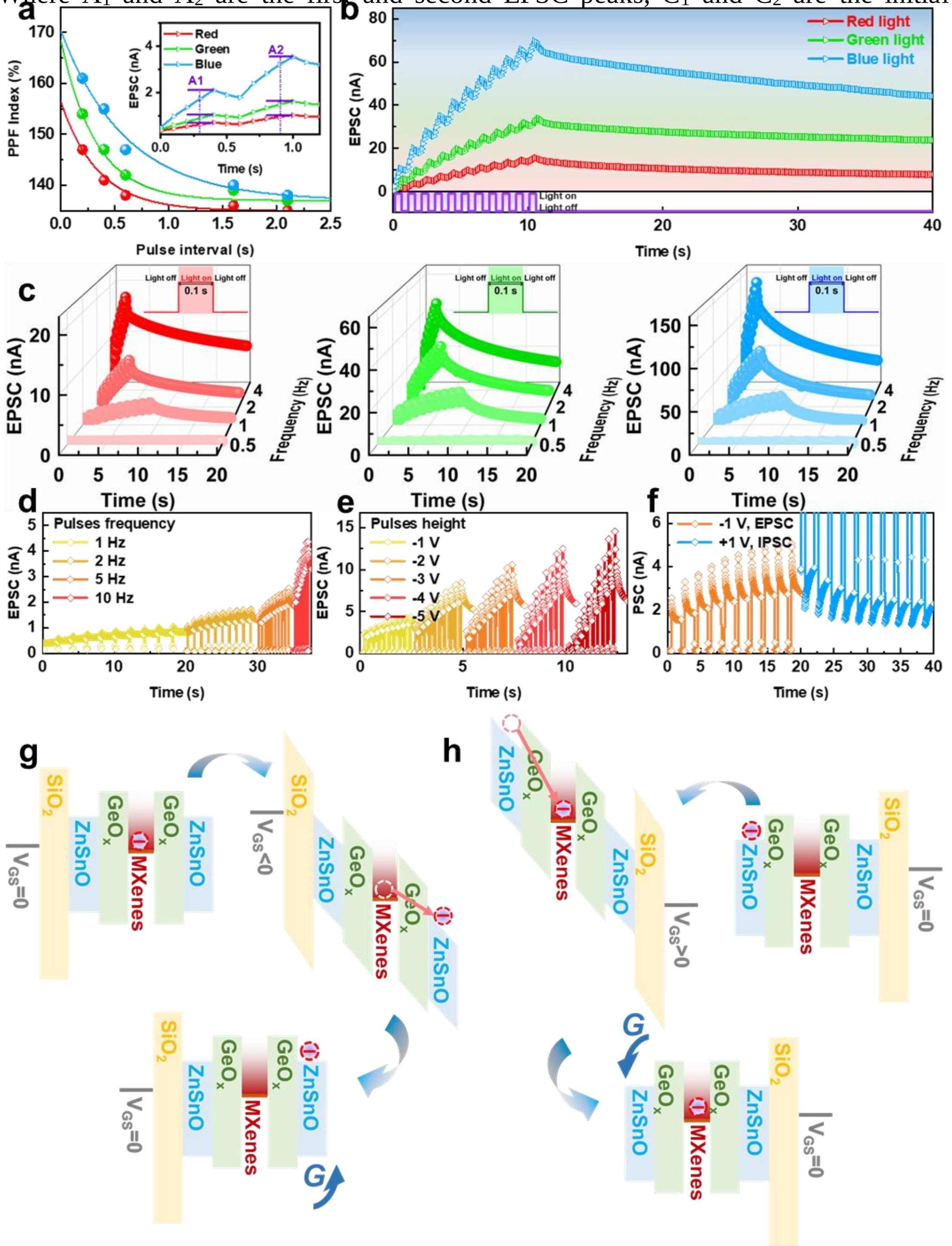

Figure 2. Synaptic behaviors under visible light and voltage stimuli. (a) PPF results of the GMXSTs under RGB light inputs. (b) EPSC behavior of the GMXSTs induced by multiple RGB incident light spikes. (c) Frequency-adjusted synaptic behaviors of the GMXSTs under RGB RGB light stimuli. The electrical induced EPSC behaviors of the GMXSTs adjusted by (d) V_{GS} pulse frequency and (e) V_{GS} pulse height. (f) IPSC behavior of the GMXST generated by the positive V_{GS} pulses, representing an inhibitory mode working mode. Schematic diagram of the energy bands of the GMXSTs in two working modes: (g) excitatory and (h) inhibitory.

facilitation magnitudes, and τ_1 and τ_2 are relaxation time constants. The fitting results of PPF index curve of blue light are $C_1 = 0.17$, $C_2 = 0.17$, $\tau_1 = 0.55$， and $\tau_2 = 0.67$. The fitting results of PPF index curve of green light are $C_1 = 0.16$, $C_2 = 0.16$, $\tau_1 = 0.29$， and τ_2= 0.35. The fitting results of PPF index curve of red light are $C_1 = 0.1$, $C_2 = 0.1$, τ_1 = 0.0.31, and $\tau_2 = 0.38$. Similar to the biological system, a shorter Δt led to a higher gain of the second peaks. Furthermore, the current gain caused by paired-pulse could be extended to a multi-spikes test, as displayed in **Figure 2**(b), where the EPSC under RGB light input was obtained by a series of 1 Hz, 500 ms spikes. The gradual increase of EPSC was observed, and it is consistent with the order of the relative magnitude of the previous RGB photogenerated current gains. The current retention phenomenon was also matched with the excitatory plasticity of biological synapses [48]. Figure S10 exhibits the variation of the EPSC under RGB spikes of 30 devices, indicating an excellent uniformity. In addition, the EPSC gain could be adjusted by the frequency of the light spikes, as shown in **Figure 2**(c). We applied the 100 ms RGB light spikes with various frequencies (0.5, 1, 2, and 4 Hz), and the devices showed a current output from low to high as the input frequency increases. This outcome was also consistent with the individual biological behavior that the more frequent stimulus leads to a more intense response. Compared with the current gain tested under 0.5 Hz input RGB light spikes, the output under 4 Hz measurement was increased by at least 10 times (under red incident light), indicating an application potential in high-pass filters [14, 49]. Interestingly, the synaptic TFTs also showed similar characteristics when replacing the GMX with pure GeO_x, as shown in Figure S11. The reason could be attributed to the existence of GeO_x/ZTO heterojunction, which is also the main reason for the photocurrent, as previously discussed. However, the EPSC for the GeO_x group was much less than the GMX based devices under the same input condition (4 Hz, 100 ms),

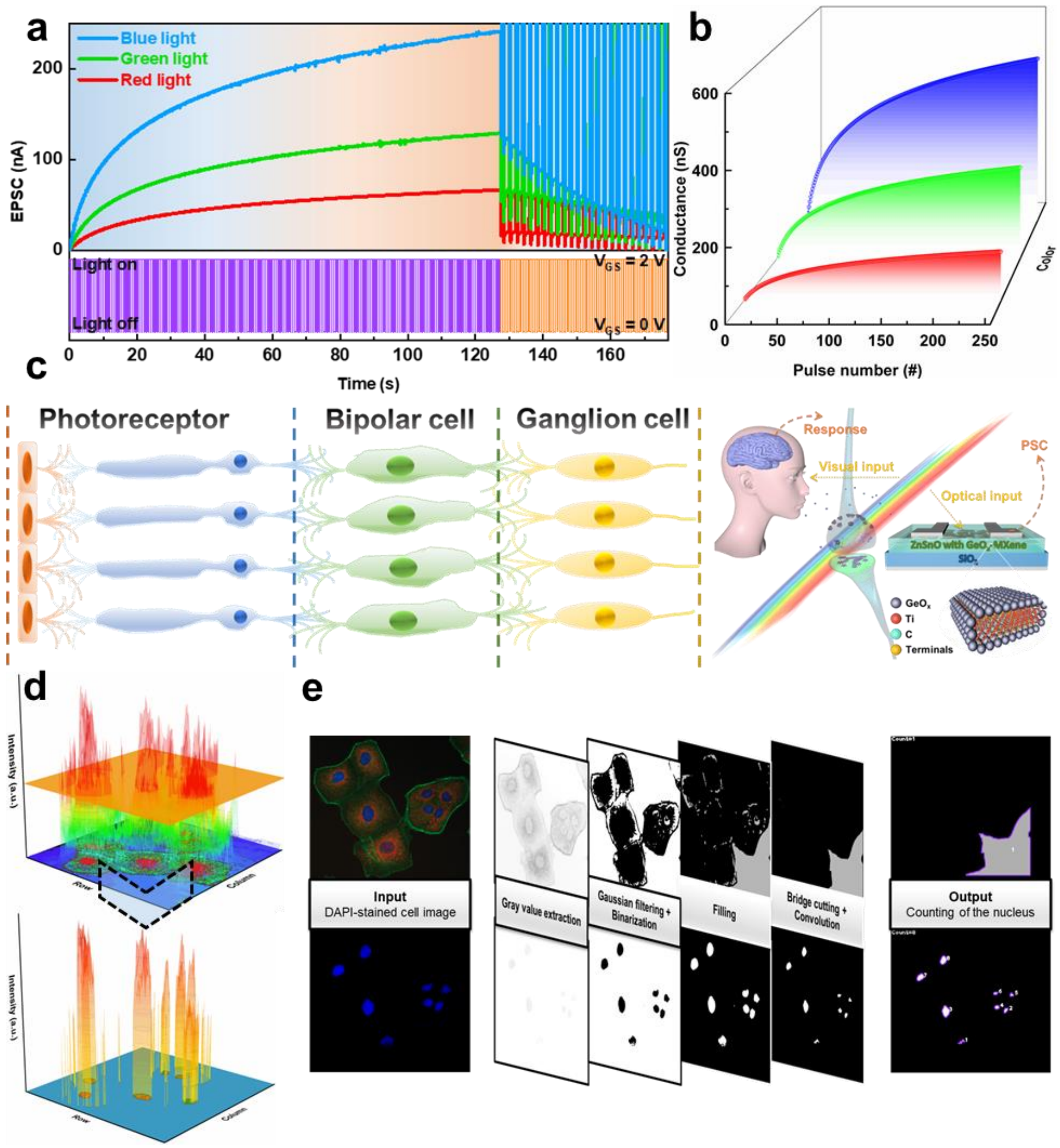

Figure 3. Visual perception applications based on photoelectric co-regulation. (a) GMXSTs write characteristics under 255 RGB pulses and erase characteristics under 50 positive V_{GS} pulses. (b) 256 G states of the devices used to represent the RGB values of images pixels. (c) EPSC output controlled by the wavelength of the incident light used to simulate the human eye's distinction between colors. (d) Schematic diagram of nucleus detection and irrelevant pixel erasure of DAPI-stained Madin-Darby cell fluorescence image . (e) Comparison of count results of DAPI stained fluorescent Madin-Darby cell images with and without the nucleus detection process .

which is another evidence that the MXene enhanced the photocurrent through electron providing and area expansion.

Moreover, the GMXSTs also showed V_{GS} pulses induced synaptic behaviors adjusted by the pulse frequency and height, as depicted in **Figure 2**(d) and (e). Under the negative input voltage pulse input from weak (low frequency and amplitude) to strong (high frequency and amplitude), the EPSC of the devices also showed a trend from low to high. Unlike the light input test, the polarity of the voltage input can change the working mode of GMXSTs. As shown in **Figure 2**(f), the negative V_{GS} pulses led to the increase of PSC representing the excitatory mode, while the positive V_{GS} pulses led to the decrease of PSC, referring to the inhibitory mode. This phenomenon could be explained by the floating gate effect formed by the MXene/GeO_x/ZTO stack structure, as shown in **Figure 2**(g) and (h), which is consistent with the previous researches [34, 40]. The channel conductance (G) of the ZTO\GMX-ZTO heterostructure could be controlled by the electron trapping and de-trapping processes in the MXene layer. Firstly, V_{GS} bias equaled to zero, a large number of electrons in the MXene layer are trapped due to the conduction band (Ec) barriers between the Mxene and GeO_x layers on both sides [40]. Secondly, during the negative V_{GS} pulse, electrons tunneled through the GeO_x into the ZTO layer due to the offset of Ec [40]. Finally, after the pulse disappeared, the carrier concentration in the ZTO channel went up, leading to a higher G value and I_{DS} [40]. On the opposite, the positive V_{GS} pulse led to a re-trapping process of the electron tunneled from ZTO to the MXene layer, and therefore the G would re-decrease to the original state [40]. As widely reported, for applicating synaptic TFTs in the field of neuromorphic computing, this rising and falling characteristic of the G controlled by V_{GS} pulses plays an important role in stimulating the nodes of the weight matrix [3].

Combining the visible-light-induced exciting work mode and the V_{GS} induced depression work mode together, the logic of "light writing and voltage erasing" would be realized, as plotted in **Figure 3**(a). 255 RGB light spikes with a frequency of 2 Hz and a width of 200 ms were applied on the GMXSTs to generate the rising EPSC. Subsequently, 50 V_{GS} pulses with 1 Hz 500 ms were utilized to erase the increased EPSC back to the initial value. Consistent with the previous description, the input of RGB light with three different wavelengths will cause the output currents with different amplitudes. Extracting the G values tuned by each light spike, the memory states of the GMXSTs stimulated by three colors of light input are shown in **Figure 3**(b).

For image processing applications, a pre-processing of distinguishing the colors of objects can effectively reduce the influence of redundant information and improve the speed and accuracy of calculations [50]. The results established a one-to-one mapping between the RGB values and the 256 G states. As the conceptual diagram plotted in **Figure 3**(c), just as human visual perception neuron system, the RGB 3-channel dividing vision sensor array could be realized according to the PSC values [51, 52]. Consequently, similar to the human eyes, the target area in the image with specific color could be detected accordingly. Figure S12 gives a simulating example of processing the image through the vision sensor array. Through setting the target interval of G to be less than 80 nS, 80-120 nS, and greater than 150 nS, the red "land", green "plant", and blue "river and sky" parts of the picture were clearly extracted. **Figure 3**(d) and (e) further introduce an application based on this kind of target component processing. Staining cell samples with chemical reagents such as DAPI is a common method in the biomedical field, where the nucleus part will be blue due to DAPI staining [53]. For counting the cells in a DAPI stained image, a pre-processing could be operated via weakening the pixels other than blue ones, and thus the nucleus would be located. For a visual sensor array based on the GMXSTs, the weakening operation could be done by the V_{GS} pulses caused erasing process. **Figure 3**(e) shows the comparison results for

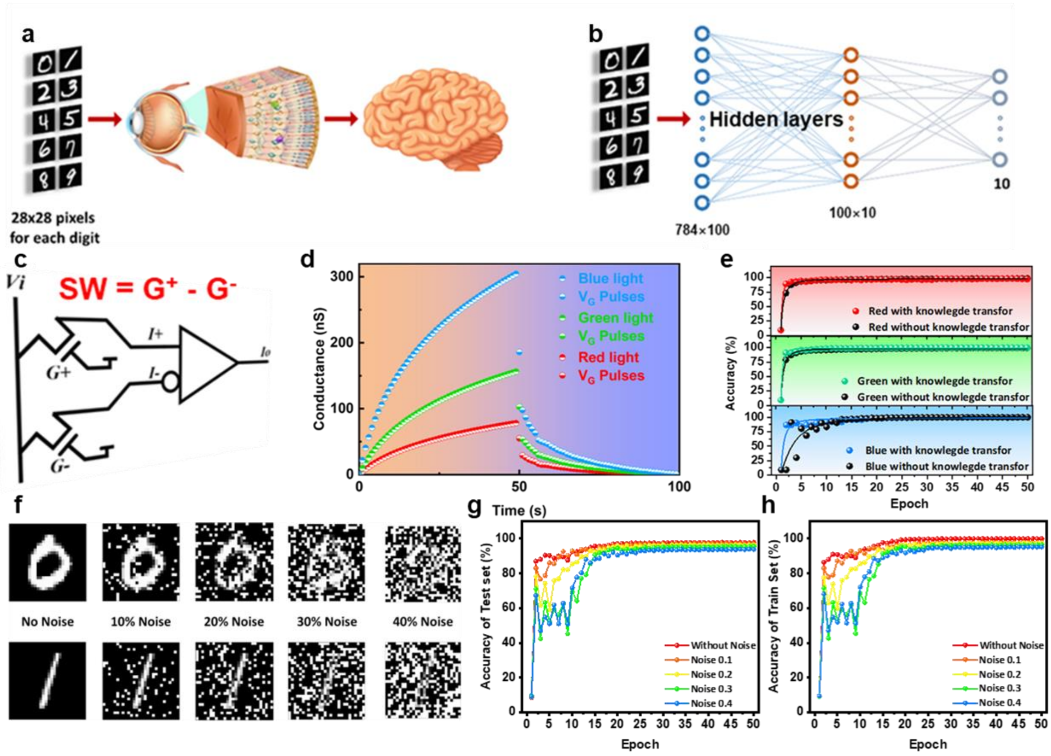

Figure 4. Applications of GMXSTs in neural network computing. The image identification systems of (a) biological individual and (b) neuromorphic computing system with ANN algorithm for MNIST hand-written digit recognition task. (c) The circuits schematic diagram of two GMXSTs for one node in SW matrix. (d) The LTP/D behavior of the GMXSTs obtained by optical writing under 50 RGB light spikes and electrical erasing under 50 positive pulses. (e) The recognition accuracy rate of the training set as training epoch increases based on three sets of LTP/D. (f) Images of digit 0 and 1 with various noise levels. The recognition accuracy rate of the g) training set and h) test set with various levels of noise as training epoch increases.

the cell count task with and without the pre-processing. The cell counter was established by a typical algorithm based on the Open CV library, including grayscale extraction, filtering, binarization, filling, bridge cutting, and convolution steps. As depicted, for a fluorescent image of a highly adhesive Madin-Darby cell, the counter failed without the pre-processing and successfully obtained the result after locating the nucleus [53].

Furthermore, to explore the in-memory computing capability, we established a classifier based on the performance of GMXSTs, which successfully complete the MNIST hand-written digit recognition task via an ANN algorithm-based simulator. The

MNIST database consists of labelled images of hand-written digits, which was divided into training set (~60000 samples) and test set (~10000 samples) in the simulation, as illustrated in Figure S13. **Figure 4**(a) displays the classification process of biological vision system for image information. To realize similar function, the ANN network converted voltages inputs referred to image pixels to 10 kinds of current outputs through the synaptic weight (SW) matrix, containing two hidden layers, as shown in **Figure 4**(b). Each node if SW matrix in ANN represented by the G difference (G^+ - G^-) between two GMXSTs, with schematic diagram principally illustrated in **Figure 4**(c) since the value of G could only be positive [21]. Furthermore, by adding knowledge transfer in the simulation process, thus greatly improves the speed of fitting convergence. Nonlinearity and discrete conductance modulation are two major difficulties in the application of synaptic transistors to artificial neural network arrays. The updating algorithm using the supervised learning mode is the back-propagation algorithm, which is more suitable for updating the array of continuous values rather than the synaptic array composed of discrete values. When using the backpropagation algorithm to update the synaptic array, the phenomenon of "over-sensitive update" will occur. In addition, the nonlinearity of the synaptic transistor will also affect the accuracy of the whole model, which is shown by the large fluctuation of the accuracy during training and the sharp decrease in the accuracy. Therefore, learned from the concept of knowledge transfer in the field of machine learning and integrated it into the training of synaptic arrays. Knowledge transfer is to use the teacher model with higher accuracy to guide and train the student model with lower accuracy. The external equipment stores the ideal conductance data Gideal, which is obtained by training the artificial neural network with software. If the conductance value of the transistor is closer to the ideal conductance value, the accuracy of the model will be higher. The external device is connected to the gate of the synaptic transistor together with the backpropagation algorithm circuit. When the backpropagation algorithm circuit returns an updated information Vinformation the external device will obtain the current conductance value G of the transistor. Vinformation>0 means the weight needs to increase, and Vinformation<0 means the weight needs to decrease (Vinformation<Vth). In this way, the influence of nonlinearity and discrete resistance of synaptic transistors on training can be reduced. The simulation results also show the effectiveness of this method.Therefore, The SW updating in ANN was realized by the updating of G in LTP/D curves. As shown in Figure S14, the LTP/D behaviours of the GMXSTs were obtained by a light-voltage mixed test. 50 RGB light spikes (2Hz) were applied to enhance the current while 50 positive gate voltages (2Hz, 1 V) led to the decrease of the current. According to the current results, the G states under RGB stimuli conditions for ANN simulation could be extracted, as depicted in **Figure 4**(d). Based the fitting results of LTP/D properties, the updating rules of G^+ AND G^- could be expressed as follow [54]:

$$\boldsymbol{G_{n+1} = G_n + \triangle G_p = G_n + \alpha_p e^{-\beta_p \frac{G_n - G_{min}}{G_{max} - G_{min}}}} \tag{1}$$

$$\boldsymbol{G_{n-1} = G_n - \triangle G_p = G_n - \alpha_p e^{-\beta_p \frac{G_n - G_{min}}{G_{max} - G_{min}}}} \tag{2}$$

where the subscripts n and $(n + 1)$ represent n^{th} and $(n + 1)^{th}$ stimulation respectively, p and n stand for potentiation and depression respectively, the variables G is the conductance, $\triangle G$ is the conductance change due to the programming or erasing operation, α is the step size in conductance of the first writing or erasing operation, β is the mapping result of a function taking the nonlinearity (NL) values of the measured LTP/D curve as input, and the parameters are illustrated as Table S1 and Table S2 [55]. The accuracy rates of the training set based on the LTP/D behaviours obtained under RGB light spikes are illustrated in **Figure 4**(e). It could be overserved that the recognition accuracy rates increase rapidly in the beginning due to the existence of knowledge transfe, and after around 5 training epochs, the recognition accuracy rates tend to reach a saturation. The final recognition accuracy rate of the training set reaches 96.8%, 98.1%, 98.3% at the 200th training epoch respectively for RGB simulated LTP/D, respectively. This result shows that the ANN based on the synaptic TFT could perform hand-written digit recognition task with a relatively high accuracy. Figure S15 shows recently published synaptic devices that required the number of epochs for convergence in the process of neural network recognition. It can be seen from the results that due to the existence of knowledge transfer, the training epoch required for recognition rate convergence is far lower than that of most published works [56-63].

Since there was not a large difference in the training results with the SW updating strategies based on RGB light stimuli, the blue light-induced LTP/D result, with the largest recognition accuracy rate at 200th train epoch, was utilized for the following discussion of simulation on the further robustness of the implementation. Figure S16 and Figure S17 illustrates gradual increase in the recognition accuracy rate of both the training set and the test set as training epoch increases. It could be observed from confusion matrixes of training and test sets that as training epoch increases, the colour of the pixels on the diagonal line becomes closer to dark blue, which means the recognition accuracy rate of each digit becomes closer to 100%. Figure S18 illustrates the recognition accuracy rate of each digit at 200th training epoch. The recognition accuracy rate of digit 5 is the lowest, slightly greater than 80% for both training and the

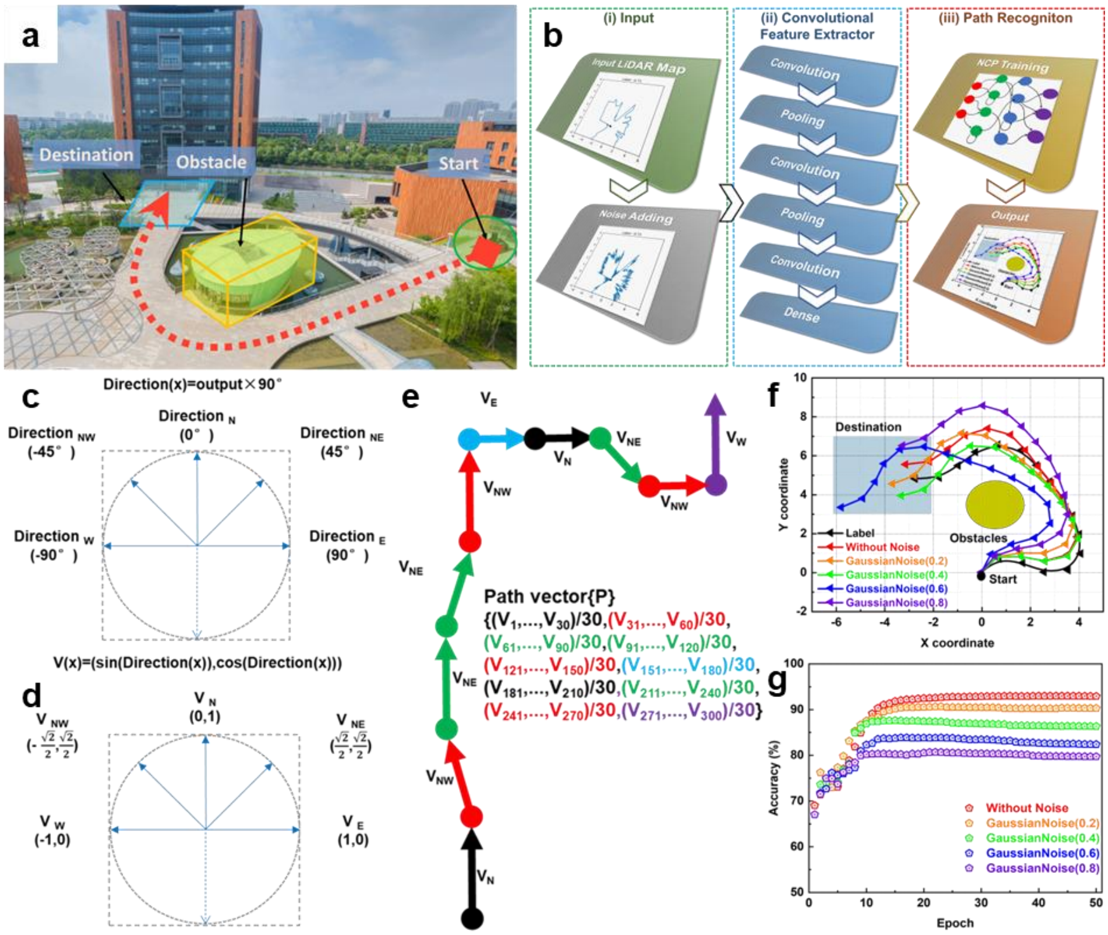

Figure 5. Applications of NCP network path recognition based on GMXSTs. (a) Schematic illustration of the path recognition task. (b) The structure of the NLP-based neural network computing system for path recognition task. (c) Vector maps and coordinates for directions. (d) The scalar of each vector set to fit a standard distance. (e) The configuration of a pathway vector (P), including thirty directional vectors. (f) The path recognition results with and w/o various standard deviations of Gaussian noises. (g) Recognition accuracy of path recognition as functions of learning epochs under different level of Gaussian noises.

test set at the 200th epoch. The main reason is that the number of samples of digit 5 is the smallest among all the digits in the dataset, as illustrated in Figure S13.

Then we investigated the noise tolerance of the ANN simulator, all the samples in the MNIST hand-written digit dataset were altered with random noise. The samples of images with noise in the training and test sets were used for the ANN training and inferring to show the fault-tolerance of the ST-based ANN. **Figure 4**(f) shows the image of 0 and 1 with various levels of noise, from 0.1 to 0.4. **Figure 4**(g) and (h) respectively show the recognition accuracy rate of the training set and test set with noise level from 0 to 0.4. It could be noticed that as the noise level increases, the ANN requires more training epochs to reach the saturation and the recognition accuracy at the saturation decreases. According to the results, the simulator could effectively recognize the image under 30 noise condition. But with a noise level of 0.4, the recognition accuracy of training set and the test set are both around 0.4, which is also difficult to identify the number by human eyes, as depicted in Figure S19. Therefore, to some extent, the classifier is close to the image recognition ability of the human eye.

The ANN simulator based on the performance of GMXSTs showed basic application results in the field of deep learning. To reveal a more advanced application potential of GMXSTs, we applied the blue light stimulated updating rule to the task of path recognition task, as shown in **Figure 5**(a). A system based on a convolution feature extractor and an NCP path recognition unit was established to analysis the *icra2020_lidar_collision_avoidance* dataset[64]. The weight update rule is the same as that described in Figure 4. Due to the synaptic transistor neural network and digital neural network being mapped, a random number of LTP stimulation (LTP 0~5) is applied to each weight in the initialization phase, which simulates the random initialization phase of the digital neural network, making the gradient easier to calculate. Next, the update direction of each weight is through simulation calculation, but the update value and update behavior are determined by the LTP/LTD characteristics, where G_{max} is the maximum value of conductivity equal to 304.4. G_{min} is the minimum value of conductivity value equal to 0.97. G_n is the current conductivity value, and the initial G_n is G_{min}. α_P is the step length of the first update equal to 21.07. β_P is the nonlinearity equal to 5.048. This stage simulates the weight modulation process of the synaptic transistor by the peripheral circuit. For the convolution feature extractor, a one-dimensional convolution kernel with a size of 5 was used to repeatedly operate the convolution process. Combined with the pooling steps and the dense layer, which acted as a fully connected layer, the image feature was effectively extracted. Subsequently, the recurrent neural network (RNN)-like NCP neural network was utilized to train, which contained only 19 control neurons (12 interneurons, six command neurons and one action neuron). Through 253 synapses, the control neurons could reflect the convolution input to the final output. Figures 5(c) and (d) depict the method of building a path from the NCP output with the help of vectors for eight directions. The configuration of a pathway vector (P) is composed of thirty directional vectors, as shown in Figure 5(e). The direction of the turning angle at the beginning of the n_{th} vector (P_n) depends on the turning Angle at the end of P_{n-1}. Thanks to the small scale of neurons in the NCP network, the path recognition system had excellent robustness[64]. The Gaussian noises with the standard deviations of 0.2, 0.4, 0.6, and 0.8 were added to the input data, and the results of path recognition are shown in Figures 5(f) and (g). The over 80% accuracy under Gaussian noises with 0.8 standard deviations demonstrated the high noise tolerance of the NCP-based path recognition system.

3. Conclusion

In conclusion, we successfully proposed a kind of optical synaptic TFTs with enhanced photosensitivity via GMX 2D nanosheet. The existence of GeO_x/ZTO heterostructure and the V_o's excitation acted as the main factors of generating the non-volatile photocurrent. The MXene core effectively enlarged the light-receiving area of the GMX nanosheets and increased the conductivity of the channel. Through experimental demonstration, the channel structure of ZTO\GMX(freeze-dried) doped ZTO was regarded as the optimal structure for the GMXSTs. Subsequently, the RGB light spiking test and the V_{GS} pulse test were applied to the GMXSTs to reveal the synaptic behaviors. Through further exploration and analysis, the devices showed the capability of applicating in the image processing tasks. The results of nucleus detection for DAPI-stained cell counting and image reconstructions provided evidence of the GMXSTs for the applicating potential in the artificial visual perception. Finally, the LTP/D properties of RGB-voltage stimulated GMXSTs were applied to the neural network computing tasks. The results of ANN-based MNIST digits identification and NCP-based path recognition showed excellent accuracy and noise tolerance, which further provide evidence for the application potential of GMXSTs in the field of in-memory computing tasks.

4. Experimental Section

Preparation of the $Ti_3C_2T_x$ MXene dispersion. First, 2 g lithium fluoride (LiF, 99.99% metals basis, Aladdin) and 40 ml hydrochloric acid (HCl, AR 36.0~38.0%, Sinopharm Chemical Reagent Co., Ltd) were mixed and stirred in a polytetrafluoroethylene (PTFE) beaker for 30 min. Second, 2 g titanium aluminum carbide MAX (MAX-Ti_3AlC_2, 98%, 11 technology Co., Ltd) was slowly added to the beaker in the first step, the reaction temperature was adjusted to 35 °C, and stirring was continued for 24 h in a fume hood. Subsequently, the obtained solution was centrifuged (3500 rpm, 10 min) and poured off the supernatant. Then 40 ml of deionized (DI) water was added to the sediment of the centrifuge tubes. After that, the tubes were shaken by hand to mix the sediment with DI water and ultrasonicated for 15 min in a high-power ultrasonic machine (750 W). Then, the above centrifugation and ultrasonication steps were repeated until the pH of the supernatant poured out after centrifugation was 5. After that, 40 ml of ethanol (CH_3CH_2OH, AR ≥99.7%, Sinopharm Chemical Reagent Co., Ltd) was added to the centrifuge tubes, followed by ultrasonication for 1.5 h (with the function of intercalator) and centrifugation for 10 min (10000 rpm). Next, 20ml of DI water was added to the centrifuged sediment and ultrasonicated for 20 minutes. Finally, the obtained mixture was centrifuged again at 3500 rpm for 3 min to obtain the black-brown few-layer dispersion.

Preparation of the GeO_x/GMX precursors. Firstly, 0.5g of GeO_2 powder (99.99% metal basis, Aladdin) was slowly added to 5ml DI-water at 75 °C and then followed by adding the 2.5 ml ammonia (13.2 mol L^{-1}, Aladdin) into the GeO_2 suspension. The GeO_2/ammonia mixture would quickly transfer to a transparent solution, along with adding ammonia. Meanwhile, ultrasonication dispersed the 0.03g PVP (99% Aladdin) into 25ml of $Ti_3C_2T_x$ MXene dispersion (10mg ml^{-1}). After that, the PVP/MXene dispersion was added to the GeO_2/ammonia mixture with further stirring treatment. Then, the $NaBH_4$ solution (0.9g $NaBH_4$, 98% from Aladdin, added into 20 ml DI-water with ice-water bath) was slowly dropped into the above mixture solution with magnetic stirring. After 12 hours, the dark-green suspension was obtained. The GMX powder was collected in the final step after centrifuging, washing, and freeze-drying for 48h. The same approach prepared the pure GeO_x powder except for the addition of MXene nanosheet.

Preparation of the ZTO, GeO_x-ZTO, GMX-ZTO, MXene, GeO_x, GMX precursors. For the ZTO solution preparation, the HCl was first diluted 10 times with DI water. Then, 0.9 g tin chloride dihydrate ($SnCl_2{\cdot}2H_2O$, 99.99% metals basis, Aladdin) and 1.78 g zinc nitrate hexahydrate ($Zn(NO_3)_2{\cdot}6H_2O$, 99.99% metals basis, Aladdin) were added into the diluted HCl solution to obtain the pristine ZTO precursor solution. The solution was then stirred in the atmosphere for 12 h in a fume hood. For the GeO_x-ZTO/GMX-ZTO solution, the GeO_x/GMX power obtained in the previous step was added into the ZTO solution with a concentration of 0.2 mg/ml and stirred for

2 h. As control groups, the MXene dispersion and GeO_x/GMX powder were also soluted or added into DI water to form a 0.2 mg/ml solution.

Device fabrication. The heavily doped n-type silicon substrates with 100 nm thermally grown silicon oxide (SiO_2) were performed as the gate electrodes and the TFT dielectrics. A 30 min-air plasma process was applied on the SiO_2 surfaces to improve the hydrophilicity. For the channels with different structures, the depositing parameters of each kind of solution are: (i) spin-coating at 5000 rpm, 30 s, followed by pre-annealing at 180 ℃, 2 min and annealing at 300 ℃, 2 h for ZTO/GMX-ZTO/GeOx-ZTO precursors; (ii) spin-coating at 3000 rpm, 20 s and annealing at 50 ℃, 2 min for Mxene/GeO_x/GMX precursors. Finally, aluminum (Al) source and drain electrodes were deposited onto the top semiconductor layer by thermal evaporation through a shadow mask with a width/length ratio (W/L) of 15.

Characterization. The XPS measurement of the thin films was measured by Thermo scientific ESCALAB 250Xi with Al Ka X-ray source. The micro-scope of the flims was revealed by a field-emission SEM (FE-SEM, Hitachi S-4800). The microstructure and morphologies of the achieved samples were examined under the high-resolution transmission electron microscopy (HR-TEM, FEI Tecnai G2 F20 S-TWIN). The electrical characteristics of the TFTs were revealed utilizing a semiconductor analyzer (Keysight B1500 Å) at room temperature. The light spikes were provided by a pulse generator (RIGOL DG1022U)and three LED lights with RGB colors. The open-source code for the main part of NCP-based based simulation could be downloaded from https://github.com/HelloLeexy/HDF-based-Simulation

Acknowledgements

T. Zhao, Y. Cao and C. Liu contributed equally to this work. This research was funded in part by the National Natural Science Foundation of China (No. 62204210), the Natural Science Foundation of Jiangsu Province (No. BK20220284), the Natural Science Foundation of the Higher Education Institutions of Jiangsu Province (No. 22KJB510013）, the Natural Science Foundation of the Jiangsu Higher Education Institutions of China Program (No. 19KJB510059), the Suzhou Science and Technology Development Planning Project: Key Industrial Technology Innovation (No. SYG201924), University Research Development Fund (No. RDF-17-01-13), and the Key Program Special Fund in XJTLU (No. KSF-T-03, KSF-A-07). This work was partially supported by the XJTLU AI University Research Centre and Jiangsu (Provincial) Data Science and Cognitive Computational Engineering Research Centre at XJTLU, Collaborative Innovation Center of Suzhou Nano Science & Technology, the 111 Project and Joint International Research Laboratory of Carbon-Based Functional Materials and Devices.

Conflict of Interests

The authors declare no competing interests.

References

[1] D. Ham, H. Park, S. Hwang, K. Kim, Neuromorphic electronics based on copying and pasting the brain, Nat. Electron., 4 (2021) 635-644.

[2] Y. Sun, Y. Ding, D. Xie, Mixed-Dimensional Van der Waals Heterostructures Enabled Optoelectronic Synaptic Devices for Neuromorphic Applications, Adv. Funct. Mater., (2021) 2105625.

[3] L. Yin, R. Cheng, Y. Wen, C. Liu, J. He, Emerging 2D Memory Devices for In-Memory Computing, Adv. Mater., (2021) 2007081.

[4] J.Q. Yang, R. Wang, Y. Ren, J.Y. Mao, Z.P. Wang, Y. Zhou, S.T. Han, Neuromorphic Engineering: From Biological to Spike-Based Hardware Nervous Systems, Adv. Mater., 32 (2020) 2003610.

[5] H. Tan, Y. Zhou, Q. Tao, J. Rosen, S. van Dijken, Bioinspired multisensory neural network with crossmodal integration and recognition, Nat. Commun., 12 (2021) 1-9.
[6] S.Z. Bisri, S. Shimizu, M. Nakano, Y. Iwasa, Endeavor of iontronics: from fundamentals to applications of ion-controlled electronics, Advanced Materials, 29 (2017) 1607054.
[7] I.H. Im, S.J. Kim, H.W. Jang, Memristive Devices for New Computing Paradigms, Advanced Intelligent Systems, 2 (2020).
[8] K.J. Kwak, D.E. Lee, S.J. Kim, H.W. Jang, Halide Perovskites for Memristive Data Storage and Artificial Synapses, J Phys Chem Lett, 12 (2021) 8999-9010.
[9] K. Lu, X. Li, Q. Sun, X. Pang, J. Chen, T. Minari, X. Liu, Y. Song, Solution-processed electronics for artificial synapses, Mater. Horiz., 8 (2021) 447-470.
[10] D.O. Hebb, The organization of behavior: A neuropsychological theory, Psychology Press, 2005.
[11] L.O.M. Chua, The missing circuit element. circuit theory, IEEE Trans, 18 (1971) 507-519.
[12] P. Hasler, C. Diorio, B.A. Minch, C. Mead, Single transistor learning synapses, (1995).
[13] S.J. Kim, S.B. Kim, H.W. Jang, Competing memristors for brain-inspired computing, iScience, 24 (2021) 101889.
[14] C. Zhang, S. Wang, X. Zhao, Y. Yang, Y. Tong, M. Zhang, Q. Tang, Y. Liu, Sub-Femtojoule-Energy-Consumption Conformable Synaptic Transistors Based on Organic Single-Crystalline Nanoribbons, Adv. Funct. Mater., 31 (2021) 2007894.
[15] L. Yin, W. Huang, R. Xiao, W. Peng, Y. Zhu, Y. Zhang, X. Pi, D. Yang, Optically stimulated synaptic devices based on the hybrid structure of silicon nanomembrane and perovskite, Nano Lett., 20 (2020) 3378-3387.

[16] S. Cohen-Cory, The developing synapse: construction and modulation of synaptic structures and circuits, Science, 298 (2002) 770-776.

[17] S. Seo, B.-S. Kang, J.-J. Lee, H.-J. Ryu, S. Kim, H. Kim, S. Oh, J. Shim, K. Heo, S. Oh, Artificial van der Waals hybrid synapse and its application to acoustic pattern recognition, Nature communications, 11 (2020) 1-9.

[18] J. Yu, G. Gao, J. Huang, X. Yang, J. Han, H. Zhang, Y. Chen, C. Zhao, Q. Sun, Z.L. Wang, Contact-electrification-activated artificial afferents at femtojoule energy, Nat. Commun., 12 (2021) 1-10.

[19] D. Jayachandran, A. Oberoi, A. Sebastian, T.H. Choudhury, B. Shankar, J.M. Redwing, S.J.N.E. Das, A low-power biomimetic collision detector based on an in-memory molybdenum disulfide photodetector, 3 (2020) 646-655.

[20] J. Sun, S. Oh, Y. Choi, S. Seo, M.J. Oh, M. Lee, W.B. Lee, P.J. Yoo, J.H. Cho, J.H. Park, Optoelectronic Synapse Based on IGZO-Alkylated Graphene Oxide Hybrid Structure, Advanced Functional Materials, 28 (2018) 1804397.

[21] Y. Wang, Q. Liao, D. She, Z. Lv, Y. Gong, G. Ding, W. Ye, J. Chen, Z. Xiong, G. Wang, Modulation of binary neuroplasticity in a heterojunction-based ambipolar transistor, ACS Applied Materials & Interfaces, 12 (2020) 15370-15379.

[22] J.J. Yang, D.B. Strukov, D.R. Stewart, Memristive devices for computing, Nat. Nanotechnol., 8 (2013) 13-24.

[23] C.S. Yang, D.S. Shang, N. Liu, G. Shi, X. Shen, R.C. Yu, Y.Q. Li, Y. Sun, A Synaptic Transistor based on Quasi-2D Molybdenum Oxide, Adv. Mater., 29 (2017) 1700906.

[24] S.W. Cho, S.M. Kwon, Y.-H. Kim, S.K.J.A.I.S. Park, Recent progress in transistor-based optoelectronic synapses: from neuromorphic computing to artificial sensory system, 3 (2021) 2000162.

[25] Y. Lee, J.Y. Oh, W. Xu, O. Kim, T.R. Kim, J. Kang, Y. Kim, D. Son, J.B.-H. Tok, M.J.J.S.a. Park, Stretchable organic optoelectronic sensorimotor synapse, 4 (2018) eaat7387.

[26] Z. Zhang, S. Wang, C. Liu, R. Xie, W. Hu, P. Zhou, All-in-one two-dimensional retinomorphic hardware device for motion detection and recognition, Nat. Nanotechnol., (2021) 1-6.

[27] W. Jin, P.-C. Yeh, N. Zaki, D. Zhang, J.T. Sadowski, A. Al-Mahboob, A.M. van Der Zande, D.A. Chenet, J.I. Dadap, I.P. Herman, Direct measurement of the thickness-dependent electronic band structure of MoS 2 using angle-resolved photoemission spectroscopy, Phys. Rev. Lett., 111 (2013) 106801.

[28] A.K. Geim, I.V. Grigorieva, Van der Waals heterostructures, Nature, 499 (2013) 419-425.

[29] Y. Liu, N.O. Weiss, X. Duan, H.-C. Cheng, Y. Huang, X. Duan, Van der Waals heterostructures and devices, Nat. Rev. Mater., 1 (2016) 1-17.

[30] M. Buscema, J.O. Island, D.J. Groenendijk, S.I. Blanter, G.A. Steele, H.S. van der Zant, A. Castellanos-Gomez, Photocurrent generation with two-dimensional van der Waals semiconductors, Chem. Soc. Rev., 44 (2015) 3691-3718.

[31] G. Cao, P. Meng, J. Chen, H. Liu, R. Bian, C. Zhu, F. Liu, Z. Liu, 2D Material Based Synaptic Devices for Neuromorphic Computing, Adv. Funct. Mater., 31 (2020).

[32] S.J. Kim, T.H. Lee, J.-M. Yang, J.W. Yang, Y.J. Lee, M.-J. Choi, S.A. Lee, J.M. Suh, K.J. Kwak, J.H. Baek, I.H. Im, D.E. Lee, J.Y. Kim, J. Kim, J.S. Han, S.Y. Kim, D. Lee, N.-G. Park, H.W. Jang, Vertically aligned two-dimensional halide perovskites for reliably operable artificial synapses, Mater. Today, 52 (2022) 19-30.

[33] L. Mennel, J. Symonowicz, S. Wachter, D.K. Polyushkin, A.J. Molina-Mendoza, T.J.N. Mueller, Ultrafast machine vision with 2D material neural network image sensors, 579 (2020) 62-66.

[34] B. Lyu, Y. Choi, H. Jing, C. Qian, H. Kang, S. Lee, J.H. Cho, 2D MXene–TiO2 Core–Shell Nanosheets as a Data-Storage Medium in Memory Devices, Advanced Materials, 32 (2020) 1907633.

[35] J. Li, Y. Du, C. Huo, S. Wang, C. Cui, Thermal stability of two-dimensional Ti2C nanosheets, Ceramics International, 41 (2015) 2631-2635.

[36] B. Anasori, M.R. Lukatskaya, Y. Gogotsi, 2D metal carbides and nitrides (MXenes) for energy storage, Nature Reviews Materials, 2 (2017) 1-17.

[37] B. Xu, M. Zhu, W. Zhang, X. Zhen, Z. Pei, Q. Xue, C. Zhi, P. Shi, Ultrathin MXene-micropattern-based field-effect transistor for probing neural activity, Advanced Materials, 28 (2016) 3333-3339.

[38] C. Zhang, Y. Ma, X. Zhang, S. Abdolhosseinzadeh, H. Sheng, W. Lan, A. Pakdel, J. Heier, F. Nüesch, Two-dimensional transition metal carbides and nitrides (MXenes): synthesis, properties, and electrochemical energy storage applications, Energy & Environmental Materials, 3 (2020) 29-55.

[39] A. Agresti, A. Pazniak, S. Pescetelli, A. Di Vito, D. Rossi, A. Pecchia, M.A. der Maur, A. Liedl, R. Larciprete, D.V. Kuznetsov, Titanium-carbide MXenes for work function and interface engineering in perovskite solar cells, Nature materials, 18 (2019) 1228-1234.

[40] T. Zhao, C. Zhao, W. Xu, Y. Liu, H. Gao, I.Z. Mitrovic, E.G. Lim, L. Yang, C.Z. Zhao, Bio-Inspired Photoelectric Artificial Synapse based on Two-Dimensional Ti3C2Tx MXenes Floating Gate, Adv. Funct. Mater., (2021) 2106000.

[41] S. Chertopalov, V.N. Mochalin, Environment-sensitive photoresponse of spontaneously partially oxidized Ti3C2 MXene thin films, ACS Nano, 12 (2018) 6109-6116.

[42] S.M. Kwon, S.W. Cho, M. Kim, J.S. Heo, Y.H. Kim, S.K. Park, Environment-Adaptable Artificial Visual Perception Behaviors Using a Light-Adjustable Optoelectronic Neuromorphic Device Array, Adv. Mater., 31 (2019) 1906433.

[43] C. Liu, Y. Zhao, R. Yi, H. Wu, W. Yang, Y. Li, I. Mitrovic, S. Taylor, P. Chalker, R. Liu, Enhanced electrochemical performance by GeOx-Coated MXene nanosheet anode in lithium-ion batteries, Electrochim. Acta, 358 (2020) 136923.

[44] J. Yu, L. Liang, L. Hu, H. Duan, W. Wu, H. Zhang, J. Gao, F. Zhuge, T. Chang, H. Cao, Optoelectronic neuromorphic thin-film transistors capable of selective attention and with ultra-low power dissipation, Nano Energy, 62 (2019) 772-780.

[45] L. Hu, J. Yang, J. Wang, P. Cheng, L.O. Chua, F. Zhuge, All-optically controlled memristor for optoelectronic neuromorphic computing, Adv. Funct. Mater., 31 (2021) 2005582.

[46] S. Hong, H. Cho, B.H. Kang, K. Park, D. Akinwande, H.J. Kim, S. Kim, Neuromorphic Active Pixel Image Sensor Array for Visual Memory, ACS Nano, 15 (2021) 15362-15370.

[47] T. Zhao, C. Liu, C. Zhao, W. Xu, Y. Liu, I.Z. Mitrovic, E.G. Lim, L. Yang, C.Z. Zhao, High-performance solution-processed Ti 3 C 2 T x MXene doped ZnSnO thin-film transistors via the formation of a two-dimensional electron gas, Journal of Materials Chemistry A, 9 (2021) 17390-17399.

[48] M. Lee, W. Lee, S. Choi, J.W. Jo, J. Kim, S.K. Park, Y.H. Kim, Brain-inspired photonic neuromorphic devices using photodynamic amorphous oxide semiconductors and their persistent photoconductivity, Adv. Mater., 29 (2017) 1700951.

[49] L. Li, X.-L. Wang, J. Pei, W.-J. Liu, X. Wu, D.W. Zhang, S.-J. Ding, Floating-gate photosensitive synaptic transistors with tunable functions for neuromorphic computing, Sci. China Mater., (2020).

[50] J. Du, D. Xie, Q. Zhang, H. Zhong, F. Meng, X. Fu, Q. Sun, H. Ni, T. Li, E.-j. Guo, A robust neuromorphic vision sensor with optical control of ferroelectric switching, Nano Energy, 89 (2021) 106439.

[51] X. Yang, J. Han, J. Yu, Y. Chen, H. Zhang, M. Ding, C. Jia, J. Sun, Q. Sun, Z.L.J.A.n. Wang, Versatile triboiontronic transistor via proton conductor, 14 (2020) 8668-8677.

[52] H.L. Park, H. Kim, D. Lim, H. Zhou, Y.H. Kim, Y. Lee, S. Park, T.W. Lee, Retina-inspired carbon nitride-based photonic synapses for selective detection of UV light, Adv. Mater., 32 (2020) 1906899.

[53] H. Wang, Q. Zhao, Z. Ni, Q. Li, H. Liu, Y. Yang, L. Wang, Y. Ran, Y. Guo, W.J.A.M. Hu, A ferroelectric/electrochemical modulated organic synapse for ultraflexible, artificial visual-perception system, 30 (2018) 1803961.

[54] T. Zhao, C. Zhao, W. Xu, Y. Liu, H. Gao, I.Z. Mitrovic, E.G. Lim, L. Yang, C.Z. Zhao, Bio-Inspired Photoelectric Artificial Synapse based on Two-Dimensional Ti3C2Tx MXenes Floating Gate, Advanced Functional Materials, 31 (2021) 2106000.

[55] R. Yu, E. Li, X. Wu, Y. Yan, W. He, L. He, J. Chen, H. Chen, T. Guo, Electret-based organic synaptic transistor for neuromorphic computing, ACS Applied Materials & Interfaces, 12 (2020) 15446-15455.

[56] J. Kim, S. Song, H. Kim, G. Yoo, S.S. Cho, J. Kim, S.K. Park, Y.-H.J.J.o.A. Kim, Compounds, Light-stimulated artificial photonic synapses based on solution-processed In-Sn-Zn-O transistors for neuromorphic applications, 903 (2022) 163873.

[57] J. Du, D. Xie, Q. Zhang, H. Zhong, F. Meng, X. Fu, Q. Sun, H. Ni, T. Li, E.-j.J.N.E. Guo, A robust neuromorphic vision sensor with optical control of ferroelectric switching, 89 (2021) 106439.

[58] J. Zhang, T. Sun, S. Zeng, D. Hao, B. Yang, S. Dai, D. Liu, L. Xiong, C. Zhao, J.J.N.E. Huang, Tailoring neuroplasticity in flexible perovskite QDs-based optoelectronic synaptic transistors by dual modes modulation, 95 (2022) 106987.

[59] X. Deng, S.Q. Wang, Y.X. Liu, N. Zhong, Y.H. He, H. Peng, P.H. Xiang, C.G.J.A.F.M. Duan, A flexible mott synaptic transistor for nociceptor simulation and neuromorphic computing, 31 (2021) 2101099.

[60] H. Li, Y. Ding, H. Qiu, Y. Zhu, C. Han, G. Liu, F. Shan, Flexible and Compatible Synaptic Transistor Based on Electrospun In2O3 Nanofibers, IEEE Trans. Electron Devices, 69 (2022) 5363-5367.

[61] C. Wang, Q. Sun, G. Peng, Y. Yan, X. Yu, E. Li, R. Yu, C. Gao, X. Zhang, S. Duan, H. Chen, J. Wu, W. Hu, CsPbBr3 quantum dots/PDVT-10 conjugated polymer hybrid film-based photonic synaptic transistors toward high-efficiency neuromorphic computing, Sci. China Mater., 65 (2022) 3077-3086.

[62] G. Li, D. Xie, H. Zhong, Z. Zhang, X. Fu, Q. Zhou, Q. Li, H. Ni, J. Wang, E.J. Guo, M. He, C. Wang, G. Yang, K. Jin, C. Ge, Photo-induced non-volatile VO(2) phase transition for neuromorphic ultraviolet sensors, Nat Commun, 13 (2022) 1729.

[63] C. Wang, H. Liu, L. Chen, H. Zhu, L. Ji, Q.-Q. Sun, D.W. Zhang, Ultralow-Power Synaptic Transistor Based on Wafer-Scale MoS2 Thin Film for Neuromorphic Application, IEEE Electron Device Lett., 42 (2021) 1555-1558.

[64] M. Lechner, R. Hasani, A. Amini, T.A. Henzinger, D. Rus, R. Grosu, Neural circuit policies enabling auditable autonomy, Nature Machine Intelligence, 2 (2020) 642-652.